Multi-objective Reference Trajectory Optimisation for Improved Accuracy and Throughput of High-tech Mechatronics Motion Systems

D. Kostić[1], Y.R. Tsai[2], Y.L. Tsai[2], M. Haghi[1], J. Gerritsen[1], K.W. Yan[1], W. Laarakkers[1], G. Knippels[1]

[1]ASMPT Limited, Center of Competency, The Netherlands

[2]ASMPT Limited, Taiwan

dragan.kostic@asmpt.com

Abstract

In the high-tech mechatronics equipment business, there is an everlasting ambition to achieve higher machine throughputs and accuracies without increasing hardware costs. This requires the optimization of all elements of the motion control systems used in these machines: 1) algorithms that generate reference trajectories for the motion systems, 2) feedforward and feedback motion control algorithms, and 3) hardware and software implementations of these algorithms. In this contribution, the focus is only on optimisation of the reference trajectories that we also refer to as the reference motion profiles.

In particular, the optimisation of 15-segments reference trajectories, as depicted in Figure 1, is considered. The equations to compute position $p(t)$, speed $v(t)$, acceleration $a(t)$, jerk $j(t)$ and snap $s(t)$ profiles of this trajectory, where t denotes time, can be found in [1, p 110]. Each segment $\{1, \dots, 15\}$ of such a trajectory is described by a specific polynomial function of time. Since the highest order of the polynomial function for $p(t)$ is 4, such a reference trajectory is also known as "the 4th order setpoint". In this contribution, peak values of speed (V), acceleration (A), jerk (J), and snap (S) profiles are computed by means of an optimisation algorithm. The optimisation objective is to achieve the desired point-to-point movement from the initial position P_0 to the target position P_f for the specified motion time $t_{f,spec}$, under constraints on actuator, motor drive, and voltage supply capabilities while constraining the energy content of the trajectory to minimize the amplification of position errors in the frequency range where the position controller is not capable to perform active error suppression. A similar optimisation approach can also be applied to motion profiles of lower order, e.g., linear trajectory with parabolic blends (*a.k.a.* "trapezoidal trajectory" [1, p 62], where polynomial functions of maximum 2nd-order describe a segment of the position profile) and trajectory with double S velocity profile (*a.k.a.* "the 3rd order setpoint" [1, p 79], where polynomial functions of maximum 3rd-order describe a segment of the position profile).

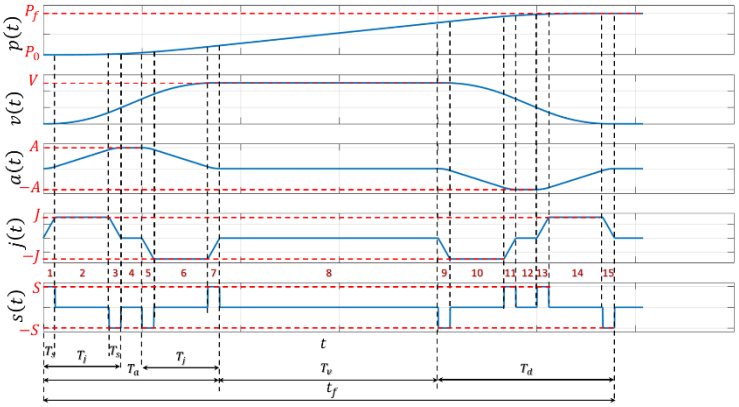

Figure 1: A 15-segments motion trajectory: position (initial at P_0, final at P_f), speed (peak value of V), acceleration (peak values of A), jerk (peak values of J), and snap (peak values of S) profiles

In Figure 2, a generic control architecture of a system with n motion axes is depicted. The dynamics in the figure incorporates the behaviour of mechanics, actuators, motor drives, feedback sensors, electronics, as well as the embedded hardware and software for feedback signal processing and control.

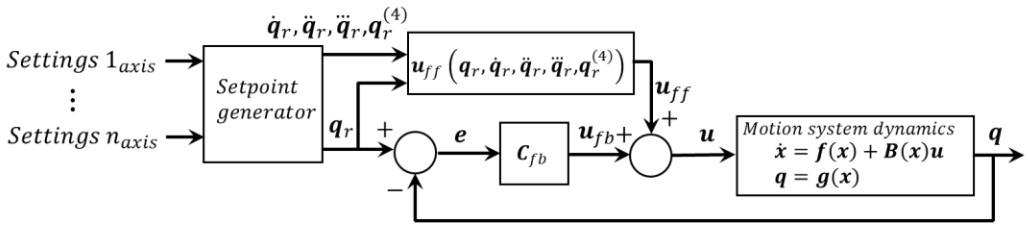

Figure 2: Generic control architecture of a motion system

Despite the degrees of freedom that represent the intended n time-dependent motions of the system

$$\boldsymbol{q} = [p_1, \dots, p_n]^T; \dot{\boldsymbol{q}} = [v_1, \dots, v_n]^T; \ddot{\boldsymbol{q}} = [a_1, \dots, a_n]^T; \boldsymbol{q}^{(4)} = [s_1, \dots, s_n]^T, \quad (1)$$

the system dynamics incorporates other time-varying state coordinates, such as motor currents and parasitic motion degrees of freedom caused by flexibilities. Therefore, variable $\boldsymbol{x} \in \mathbb{R}^m$ captures all time-varying state coordinates of the motion system, where $m > n$. For readability, the time-dependency of $\boldsymbol{x}$ is omitted for the remainder of this contribution. Since the dynamics of the motion system feature nonlinear phenomena, such as friction, position dependent inertia and kinetic effects caused by rotational axes, gravitational forces or torques, motor and motor drive dynamics, etc., a state-space representation of these dynamics contains state-dependent function $\boldsymbol{f}(\boldsymbol{x}) \in \mathbb{R}^m$ and matrix $\boldsymbol{B}(\boldsymbol{x}) \in \mathbb{R}^{m \times n}$ that model time-varying and nonlinear dynamical effects; the output function $\boldsymbol{g} \in \mathbb{R}^n$ may also be nonlinear. Only for some frictionless single-axis motion systems or rigid-body

systems with sole translational axes, it may hold that $\boldsymbol{f}(\boldsymbol{x}) = \boldsymbol{A}\boldsymbol{x}$, $\boldsymbol{A} \in \mathbb{R}^{m\times m}$. For these specific systems, matrices $\boldsymbol{A}$ and $\boldsymbol{B}$ are constant for any $\boldsymbol{x}$. On the other hand, in many cases it holds $\boldsymbol{g}(\boldsymbol{x}) = \boldsymbol{C}\boldsymbol{x}$, $\boldsymbol{C} \in \mathbb{R}^{n\times m}$ with $\boldsymbol{C}$ being constant for any $\boldsymbol{x}$. Input $\boldsymbol{u} \in \mathbb{R}^n$ (force or torque) to the system dynamics is generated by feedback $\boldsymbol{u}_{fb} \in \mathbb{R}^n$ and feedforward $\boldsymbol{u}_{ff} \in \mathbb{R}^n$ control laws, where $\boldsymbol{u}_{fb}$ is the output of feedback controller $\boldsymbol{C}_{fb}$. Input to $\boldsymbol{C}_{fb}$ is the position error $\boldsymbol{e} = \boldsymbol{q}_r - \boldsymbol{q}$. The feedforward signal $\boldsymbol{u}_{ff}$ is commonly determined based on $\boldsymbol{q}_r(t), \dot{\boldsymbol{q}}_r(t), \ddot{\boldsymbol{q}}_r(t), \dddot{\boldsymbol{q}}_r(t), \boldsymbol{q}_r^{(4)}(t)$ that represent reference profiles for the controlled system motion coordinates $\boldsymbol{q}$. These reference profiles are computed by the 15-segments setpoint generator which implements specific polynomial functions for $p_i(t)$, $v_i(t)$, $a_i(t)$, $j_i(t)$, and $s_i(t)$, $i \in \{1,2,\dots,n\}$ at each segment indicated in Figure 1, while accommodating motion specifications and constraints denoted in Figure 2 as $Settings$. The specifications and the constraints for motion axis i are:

$$Settings\ i_{axis} = \{P_0^i, P_f^i, t_{f,spec}^i, V_{lim}^i, A_{lim}^i, J_{lim}^i, S_{lim}^i, u_{lim}^i, u_{rms,lim}^i, I_{lim}^i, I_{rms,lim}^i, U_{lim}^i, C_{PSDa,lim}^i, f_1, f_2, \boldsymbol{p}^i\}, \quad (2)$$

where P_0^i and P_f^i are the initial and target positions, $t_{f,spec}^i$ is the specified motion time, V_{lim}^i, A_{lim}^i, J_{lim}^i, and S_{lim}^i are the limits on V_i, A_i, J_i, and S_i (denoted in Figure 1 without index i), respectively, u_{lim}^i and $u_{rms,lim}^i$ are the limits on the peak absolute and root-mean-squares (rms) values of system input u_i (force or torque), respectively, I_{lim}^i and $I_{rms,lim}^i$ are the limits on the peak and rms values of the motor coil currents, respectively, and U_{lim}^i is the voltage limit of the power supply. Both (DC and AC) rotary and linear electrical actuators are considered, including permanent magnet synchronous motors (PMSM). In (2), $C_{PSDa,lim}^i$ denotes a limit on the energy content of the reference acceleration profile $a_r(t)$, which is expressed in terms of the limit on the Cumulative Power Spectrum Density (CPSD) of $a_r(t)$ [2] in a frequency range $f_1 \le f \le f_2$, f is frequency in [Hz], where the motion controller cannot achieve error suppression; $\boldsymbol{p}^i$ denotes a vector of all mechanical and electrical system parameters for axis i, such as mass, coordinates of center of masses, mass moments of inertia, stiffness, damping and friction parameters, motor coil resistance and inductance, back-emf and motor force/torque constants, number of motor poles, pole pitches, etc. Settings in (2) are normally specified by a systems engineer or mechatronics system architect based on their understandings of motion system's mechanics, electronics, and actuation requirements and limits.

For mathematical formulation of the considered optimisation problem, one should observe the time-periods of different segments of the 15$^{\text{th}}$-segment trajectory depicted in Figure 1: T_a, T_j and T_s are periods of non-zero acceleration, jerk and snap, respectively, and T_v is the period of constant speed. In

this contribution we only consider 15th-segment trajectories whose position profiles are symmetric with respect to mid-point between P_0 and P_f. This consideration implies the same peak values of acceleration, jerk, and snap profiles together with equal periods of acceleration and deacceleration. Based on relations between $P_f - P_0$, V, A, J, and S on one side and T_v, T_a, T_j and T_s, on another, one can determine a total duration t_f of the 15th-segment trajectory [1, p 108]:

$$t_f = \frac{P_f - P_0}{V} + \frac{V}{A} + \frac{A}{J} + \frac{J}{S}. \tag{3}$$

The optimisation problem is posed as follows: Given the specified (target) motion time $t_{f,spec}$, determine peak values $V > 0$, $A > 0$, $J > 0$, and $S > 0$ of the 15th-segment trajectory between terminal positions P_0 and P_f such as to minimize the following cost function:

$$\mathcal{J} = \min_{\{V,A,J,S\}} \left| t_f - t_{f,spec} \right|, \tag{4}$$

while satisfying the following constraints:

$$A \geq \frac{J^2}{S}, \quad V \geq \frac{A^2}{J} + \frac{A \cdot J}{S}, \quad \text{and} \quad \frac{V}{A} + \frac{A}{J} + \frac{J}{S} \leq \frac{P_f - P_0}{V}; \tag{5}$$

$$p(0) = P_0, \quad p(t_f) = P_f, \quad V \leq V_{lim}, \quad A \leq A_{lim}, \quad J \leq J_{lim}, \quad S \leq S_{lim}; \tag{6}$$

$$|u(t)| \leq u_{lim}, \quad rms(u(t)) \leq u_{rms,lim}, \quad |i_\alpha(t)| \leq I_{lim}, \quad rms(i_\alpha(t)) \leq I_{rms,lim}$$
(α is motor coil index; e.g. $\alpha \in \{a, b, c\}$ for 3-phase PMSM), $\quad U(t) \leq U_{lim}$; (7)

$$\int_{f_1}^{f_2} PSD_{a(t)}(f) \mathrm{d}f \leq C_{PSDa,lim}. \tag{8}$$

Constraints (5) represent feasibility conditions on tuning parameter V, A, J, and S, since their violation implies no existence of the 15-segments trajectory [1, p 109]. For instance, the first inequality in (5) ensures that the period T_j of non-zero jerk cannot be shorter than the multiple of two periods T_s of non-zero snap. In (7), $i_\alpha(t)$ denotes a current in coil α, and rms is a function which computes the root-mean-squares value of its argument. In (8), $PSD_{a(t)}(f)$ is a Power Spectrum Density (PSD) function [2] of $a_r(t)$, where f is frequency and f_1 and f_2 (already appearing in [2]) representing the start and the end frequencies, respectively, of a frequency range where the feedback motion controller may amplify position error.

Cost function (4) and constraints (5)-(8) represent a multi-objective optimisation problem which is non-convex and nonlinear with respect to tuning parameters V, A, J, and S. Constraints in (7) require the computation of $u(t)$-, $i_\alpha(t)$-, and $U(t)$-profiles that correspond to the 15-segments reference trajectory conforming to V, A, J, and S. Standard frameworks can be used to model multi-body

dynamics of the motion system and the dynamics of its actuators, drives and power supplies. For instance, Lagrange-Euler approach [3] is suitable for modelling the nominal (mostly rigid-body) dynamics of the system mechanics, while dynamics of motors, their drives and power supplies can be represented by appropriate models from the literature. For example, models of a 3-phase PMSM can be found in [4]. Using models of the system mechanics, one can compute $u(t)$. Models of motor dynamics allow for the computation of $i_\alpha(t)$- and $U(t)$-profiles. To solve the nonlinear and nonconvex optimisation problem (4) under constraints (6)-(8), an interior-point algorithm [5] is suggested in this contribution.

For illustration, the described framework for multi-objective optimisation of the 15-segments reference trajectory is applied on the turret axis of VORTEX II die-bonder [6]. This machine is produced by company ASMPT, who is the global market leader with comprehensive offering of machines for assembly and advanced packaging, offering products to various customers in the fields of optoelectronics, electronics, solar energy, automotive and other segments. A photo of the VORTEX II die-bonder is shown in Figure 3.

Figure 3: VORTEX II: high performance ASMPT LED die-bonder

Dynamics of the turret mechanics can be described by a simple model:

$$J \cdot a(t) + b \cdot v(t) + f_c \cdot \mathrm{sign}(v(t)) = u(t), \tag{9}$$

where J is mass moment of inertia of the turret, b and f_c are coefficients of viscous and Coulomb friction, respectively, and u is torque applied to the turret generated by the motor. Parameters J, b and f_c are known to ASMPT from CAD data and measurements. Since the turret is actuated by a 3-phase PMSM, a model of motor dynamics [4] is used to compute currents $i_\alpha(t)$, $\alpha\{a, b, c\}$, in the motor coils and source voltage profile $U(t)$:

$$\begin{bmatrix} i_a(t) \\ i_b(t) \end{bmatrix} = \boldsymbol{h}_1(u(t), p(t), j(t)); \qquad i_c(t) = -i_a(t) - i_b(t), \tag{10}$$

$$U(t) = h_2\big(v(t), i_a(t), i_b(t), i_c(t)\big), \tag{11}$$

where $\boldsymbol{h}_1 \in \mathbb{R}^2$ is a nonlinear vector function of motor torque, position and jerk motion profiles, while $h_2 \in \mathbb{R}$ is a nonlinear scalar function of speed motion profile and currents in the motor coils. Parameters of these models are also available in a data-base of motor characteristics of ASMPT. Models (9)-(11) are used to compute $u(t)$-,$i_a(t)$-,$i_b(t)$-,$i_c(t)$-,$U(t)$-profiles that are needed to solve the optimization problem (4) under constraints (5)-(8).

To demonstrate the importance of multi-objective 15-segements reference trajectory optimisation, the left-hand side of Figure 4 depicts the four candidate motion profiles for the turret axis of VORTEX II in different colours. In this and all consecutive figures, all numerical values are removed for confidentiality reasons. One can notice that each profile depicted in Figure 4 has two distinct phases: a motion phase of the duration t_f^{circ} or t_f^{15seg} (turret rotates from P_0 to P_f) and an idle phase of the duration t_f^{idle} (turret stands still at P_f). Sum of the durations of the motion and idle phases determines the turret cycle run time. A shorter cycle run time is favourable for a higher throughput of the turret, which directly determines the throughput of the complete machine. A ratio between the duration of the motion phase and the cycle run time defines duty cycle of the turret motor. The highest duty cycle, under which motor coils do not overheat, is wishful to maximize the machine throughput.

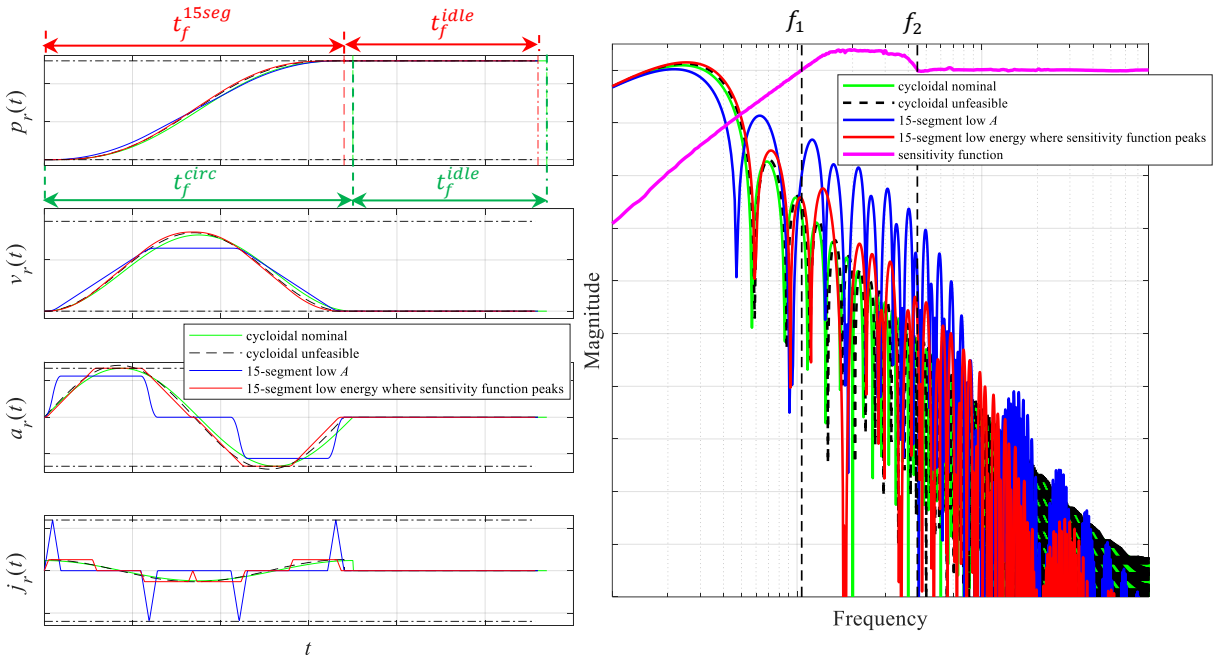

Figure 4: Left-hand side: nominal and unfeasible cycloidal, and the optimised 15-segments reference trajectories; right-hand side: sensitivity function characteristics vs. scaled PSD-plots of $a_r(t)$-profiles

By default, cycloidal trajectories [1, p 43] are used as the reference profiles for the turret axis. Examples of such trajectories are depicted in Figure 4 with green and dashed black lines. A cycloidal trajectory is appealing due to simplicity of its computation, since the same compact equations for $p_r(t)$, $v_r(t)$, $a_r(t)$, $j_r(t)$, and $s_r(t)$ are executed in the real-time reference trajectory generator at every $t \in [0, t_f]$. Furthermore, since $a_r(t)$ is a sinusoidal function of t, energy spectrum of $a_r(t)$ is only concentrated around frequency $f_{cycloidal} = 1/(2\pi t_f)$ (in [Hz]), where t_f is the duration of the motion phase. One can directly set t_f to keep the dominant energy of $a_r(t)$ below resonance frequencies of the turret dynamics. In dynamical model (9) the motor torque component which gives the largest contribution to the total torque $u_r(t)$ is linearly proportional to $a_r(t)$; therefore, $a_r(t)$ directly defines the energy content of $u_r(t)$. That can be used for mitigation of torsional vibrations in the turret mechanics, since concentration of dominant energy of the total torque away from the resonance frequencies minimizes their excitation in the motion phases of turret operation.

Among all possible cycloidal trajectories, the one depicted with green colour in Figure 4 has the shortest motion time t_f^{circ} for which all constraints (5)-(8) are met, which hereafter, is labelled as 'cycloidal nominal'. It appears that any cycloidal trajectory with a motion time $t_f < t_f^{circ}$ cannot meet all of the constraints (5)-(8) simultaneously. For motion time t_f^{15seg} of circular trajectory depicted with dashed black lines in Figure 4, $t_f^{15seg} < t_f^{circ}$ holds, and this trajectory exceeds the peak limit on the corresponding $u(t)$. Therefore, it is labelled as 'cycloidal unfeasible'. Violation of the peak limit on the turret torque can be observed by inspecting $u_r(t)$-plots shown in Figure 5. On the left-hand side in this figure, actuator related signals are plotted together with the corresponding limits indicated by horizontal dashed-dotted lines. A motor torque profile which corresponds to the 'circular unfeasible' trajectory is depicted by the dashed black line. On the right-hand side, peaks of the $u_r(t)$-profiles are enlarged to emphasize the violation of the limit on the actuator torque by the 'circular unfeasible' trajectory. One should realize that rms values of motor related signals in (7) are influenced by the duration of the idle phase of each reference trajectory in Figure 4. For maximisation of the turret duty cycle, idle phase of each trajectory is of identical duration t_f^{idle}.

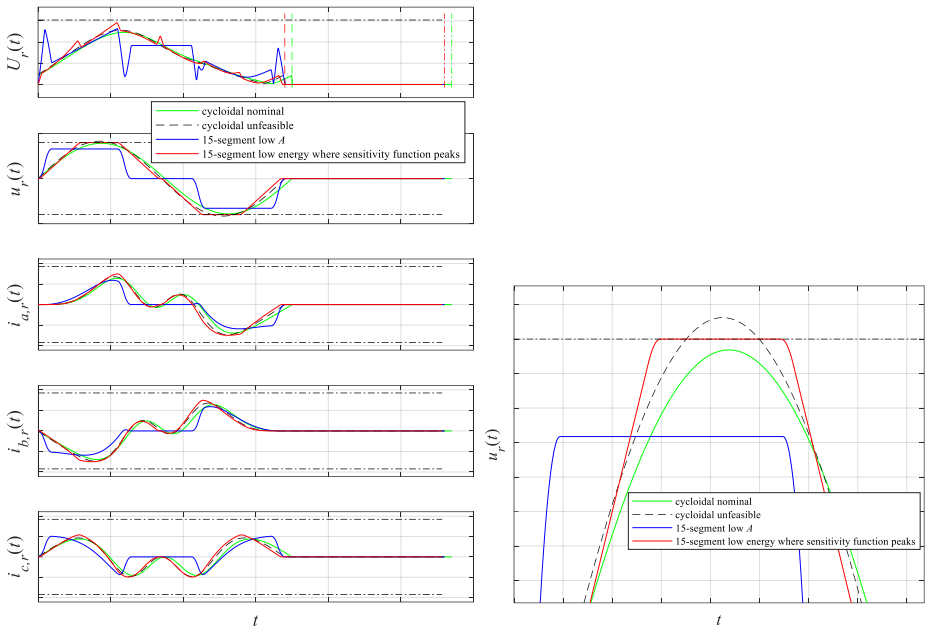

Figure 5: Left-hand side: actuator signals (input voltage $U(t)$, torque $u(t)$, and phase currents $i_a(t)$, $i_b(t)$ and $i_c(t)$); right-hand side: zoom-in reveals that peak $u(t)$ of 'unfeasible cycloidal' exceeds u_{lim}

Besides cycloidal reference trajectories, in Figure 4 two 15-segments reference trajectories are also depicted: 1) one with low peak acceleration value (A), depicted in blue colour and labelled as '15-segments low A' and 2) one with low energy in a frequency range where feedback controller may amplify position errors, depicted in red colour and labelled as '15-segments low energy where sensitivity function peaks'. Both 15-segments trajectories are computed by solving the optimisation problem (4) with constraints (5)-(7). During the computation of '15-segments low A' trajectory, condition (8) was not imposed and a value for A_{lim} was set which is lower than the value set during the computation of '15-segments low energy where sensitivity function peaks'. Condition (8) was imposed during optimisation of the trajectory depicted in red colour. For both 15-segments trajectories, the target motion time was set to $t_{f,spec} = t_f^{15seg}$. Other limits on motion profiles that are used during the optimisation are indicated in Figure 4 with horizontal dashed-dotted lines. Both optimized 15-segment trajectories achieve a target motion time t_f^{15seg}, where $t_f^{15seg} < t_f^{circ}$. A specific value for t_f^{15seg} is set to enable the throughput increase of the turret for 7%, without any changes in its hardware. Satisfaction of actuator constraints for both 15-segments trajectories can be verified by the inspection of signals shown in Figure 5 depicted in blue and red colours. All these signals lay within the imposed bounds indicated by horizontal dashed-dotted lines. A shorter motion time of the 15-segments reference trajectories is only the first prerequisite towards higher turret throughput. The second and the most critical prerequisite is to minimize settling time, meaning that right after the end of the motion phase the actual turret position $p(t)$ should converge to the reference value P_f as

quickly as possible. In other words, the position error $e(t) = P_f - p(t)$ has to remain below E_{lim}:

$$|e(t)| < E_{lim}, \quad \forall t \geq t_f^{15seg} + t_{setl}, \tag{12}$$

where t_{setl} is a settling time and E_{lim} is an accuracy limit. These values are set by process and mechatronics systems architects at ASMPT: t_{setl} is set to be much shorter in comparison to the motion time for maximizing the machine throughout; E_{lim} is set to let VORTEX II machine handle 2 mil × 4 mil (50μm × 100μm) mini LED components effectively [6]. The key difference between '15-segments low A' and '15-segments low energy where sensitivity function peaks' reference trajectories, is in their energy content illustrated by PSD characteristics [2] shown on the right-hand side in Figure 4. These PSD plots are overlayed with magnitude characteristics of the sensitivity function [7, p 193] of the turret feedback control system depicted in magenta. In the frequency domain, this sensitivity function represents a transfer function from z-transform [7, p 60] of the time-sampled reference turret position profile p_r to z-transform of the time-sampled position error $e = p_r - p$. Due to well-known 'waterbed effect' [8], pushing for a higher control bandwidth to increase frequency f_1 (indicated in the sensitivity plot on the right-hand side in Figure 4) below which magnitude of the sensitivity function is lower than 1 for active error suppression increases the magnitude of the sensitivity function above f_1. On the right-hand side in Figure 4, a frequency range where magnitude of the sensitivity function is prominently above 1 is in between frequencies f_1 and f_2. In this frequency range, the feedback controller may amplify energy content of position error e. To limit the energy content of '15-segments low energy where sensitivity function peaks' reference trajectory, condition (8) is engaged during its optimisation. A specific value of $C_{PSDa,lim}$ in (8) was set based on the frequency-domain integral of PSD function of 'cycloidal nominal' $a_r(t)$-profile in the same frequency range from f_1 to f_2. The specified $C_{PSDa,lim}$ was set higher than the calculated value of that integral to enable computation of feasible solution to the optimisation problem (4) under constraints (5)-(8). By inspecting the PSD plots overlayed with magnitude characteristics of the sensitivity function shown on the right-hand side in Figure 4, one can notice that the '15-segments low energy where sensitivity function peaks' reference trajectory depicted with red line features far less energy in the critical frequency range in between f_1 and f_2 than '15-segments low A' trajectory depicted with blue line. As a result, '15-segments low energy where sensitivity function peaks' reference trajectory should cause lower error amplification in the frequency range where magnitude of the sensitivity function is prominently above 1 than '15-segments low A'. Notify that the feasible 'cycloidal nominal' reference trajectory has the lowest energy content in between f_1 and f_2, since its energy is dominantly concentrated around frequency $1/\left(2\pi t_f^{circ}\right)$ which is well below f_1.

Figure 6 depicts the position error plots right after the end of motion phases for '15-segments low A' (depicted in blue) and '15-segments low energy where sensitivity function peaks' (depicted in red) reference trajectories. As such, these errors correspond to the settling and steady-state phases of error transients. Vertical magenta dashed line identifies the end of the allowed settling window according to formula (12). Error limits after the end of the settling window are indicated by horizontal black dashed lines. It is noticeable that '15-segments low energy where sensitivity function peaks' meets the desired steady-state accuracy within the specified settling time t_{setl}, unlike '15-segments low A'. This implies that '15-segments low energy where sensitivity function peaks' meets the accuracy prerequisite for turret throughput increase. Therefore, the turret throughput is increased by minimisation of energy content of the 15-segments trajectory in a frequency range where sensitivity function of the feedback control system indicates amplification or position errors. The optimisation method (4)-(8) is implemented in a proprietary software tool of ASMPT to facilitate and automate computation of reference trajectories for many different motion systems present in ASMPT products.

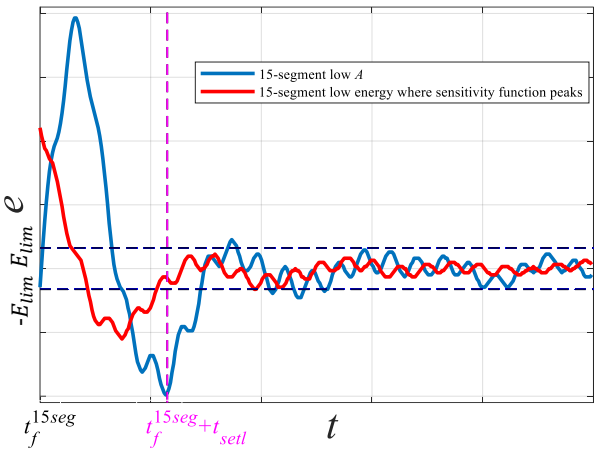

Figure 6: Setling position errors achieved with two optimised 15-segments reference trajectories

In comparison to other optimisation methods for frequency modification of reference trajectories, such as input shaping [1 p 381] and tuning peak values of the 15-segments motion profiles to eliminate the energy of the resulting 15-segments trajectory at a finite number of discrete frequencies [9], the multi-objective optimisation method does not extend the motion time of the frequency shaped trajectory. This is one of the most significant advantages of the multi-objective optimisation approach from this contribution. Its main challenge is nonlinear and nonconvex relation between tuned parameters (V, A, J, and S), on one hand, and cost function (4) and constraints (5)-(8), on another. Because of such a relation, optimisation results are very sensitive to the applied optimisation method and initial conditions due to existence of local optima of the cost function. In future, ASMPT team will explore solving problem (4)-(5) using a global optimisation method, such as DIRECT algorithm [10]. The ultimate

goal is to perform global and time-efficient optimisation of the reference trajectories to increase the throughput and accuracy of ASMPT products without hardware modifications.

References

[1] Biagiotti L and Melchiorri C 2008 *Trajectory Planning for Automatic Machines and Robots* (Berlin Heidelberg: Springer-Verlag)

[2] De Kraker B 2013 *A Numerical-Experimental Approach in Structural Dynamics* (Maastricht: Shaker Publishing B.V.) p 121

[3] Spong M W, Hutchinson S and Vidyasagar M 2020 *Robot Modeling and Control* (Wiley) p 181

[4] Beauty H W and Kirtley J L 1998 *Electric Motor Handbook* (New York: McGraw-Hill) p 166

[5] Potra F A and Stephen J W 2000 Interior-point methods *J. of Computational and Applied Mathematics* **124 (1–2)** 281–302.

[6] VORTEX II *https://semi.asmpt.com/en/products/opto-photonics/transfer_bond/da/vortex-ii/*

[7] Franklin G F, Powell J D and Workman M 1997 *Digital Control of Dynamic Systems* (Half Moon Bay: Ellis-Kagle Press)

[8] Emami-Naeini A and De Roover D 2019 Bode's Sensitivity Integral Constraints: The Waterbed Effect Revisited *ArXiv* abs/1902.11302

[9] Heertjes M, Torres J Z and Al Janaideh M 2023 Fourth-order reference trajectories in lithography stages with weakly-damped modes – a frequency-domain perspective *62nd IEEE Conf. Dec. and Control* 8696-8701

[10] Jones D R and Martins J R R A 2021 The DIRECT algorithm: 25 years later 62nd *J. Global Optim.* **79** 521-566